




RESEARCH ARTICLE | AUGUST 28 2024

# Numerical approach for the simulation of flow-induced noise around a structure with complex geometry: High-speed train bogie in a cavity

Yuan He ; David Thompson ; Zhiwei Hu 



*International Journal of Fluid Engineering* 1, 033102 (2024)

<https://doi.org/10.1063/5.0212760>



# Numerical approach for the simulation of flow-induced noise around a structure with complex geometry: High-speed train bogie in a cavity

Cite as: Int. J. Fluid Eng. 1, 033102 (2024); doi: 10.1063/5.0212760

Submitted: 6 April 2024 • Accepted: 15 July 2024 •

Published Online: 28 August 2024



View Online



Export Citation



CrossMark

Yuan He,<sup>1,a)</sup> David Thompson,<sup>1</sup> and Zhiwei Hu<sup>2</sup>

## AFFILIATIONS

<sup>1</sup>Institute of Sound and Vibration Research, Faculty of Engineering and Physical Sciences, University of Southampton, Southampton, United Kingdom

<sup>2</sup>Aerodynamics and Flight Mechanics Research Group, Faculty of Engineering and Physical Sciences, University of Southampton, Southampton, United Kingdom

<sup>a)</sup>Author to whom correspondence should be addressed: [yh6y23@soton.ac.uk](mailto:yh6y23@soton.ac.uk)

## ABSTRACT

The bogie region is a significant source of aerodynamic noise on high-speed trains. Owing to its complex geometry and flow field, numerical simulations using computational fluid dynamics are especially challenging. The main challenge is to achieve a grid with adequate resolution, especially in the boundary layer, while ensuring computational affordability. This challenge is addressed here by employing a hybrid grid, integrating a structured hexahedral mesh near solid surfaces with an unstructured polyhedral mesh in the remaining volume. To limit the number of cells in the boundary layer region, the delayed detached eddy simulation method is adopted. Additionally, to achieve a further reduction in the cell count, the Reynolds number of the model is decreased by scaling down the model size and lowering the inflow speed. The hybrid grid generation and numerical settings are guided by validated simulations of flow over cylinders. A grid sensitivity study, conducted with a simplified half-width bogie model, reveals the meshing requirements for the full-width model. Aerodynamic results highlight the rear section of the cavity and bogie as primary noise sources, emphasizing the critical role of the detached shear layer from upstream components. Time-resolved surface pressure data are input into the Ffowcs Williams–Hawkins equation for far-field noise calculation. The results indicate that the sound energy is concentrated below 200 Hz in the full-scale model, with the cavity contributing more than the bogie. This study provides a practical numerical approach for simulating a structure with complex geometry, offering insights for realistic model simulations.

© 2024 Author(s). All article content, except where otherwise noted, is licensed under a Creative Commons Attribution (CC BY) license (<https://creativecommons.org/licenses/by/4.0/>). <https://doi.org/10.1063/5.0212760>

## I. INTRODUCTION

The aerodynamic noise from high-speed trains has become more significant with increasing train speeds. Aerodynamic noise, which includes contributions from car body surfaces, inter-coach spacings, train nose, pantographs and bogies,<sup>1–6</sup> exceeds rolling noise and becomes the primary contributor to high-speed train noise above ~350 km/h.<sup>4</sup> Among these sources, the bogies contribute the greatest sound power.<sup>4</sup> Therefore, understanding the mechanisms involved in the generation of bogie noise is crucial for controlling overall aerodynamic noise from high-speed trains. However, the

complex geometry and intricate incoming flow pose significant challenges, making both experimental and numerical investigations of bogie noise extremely difficult.

Although field tests with microphone arrays can be used to localise noise sources,<sup>7</sup> they cannot readily separate the bogie aerodynamic noise from rolling noise. Additionally, field tests pose challenges such as high measurement costs and difficulties in arranging appropriate tests. Wind tunnel tests, another option, face limitations in replicating the velocity profile beneath a train, especially in low-noise wind tunnels lacking a moving ground. Uda *et al.*<sup>8</sup> addressed

this by employing an array of hot-wire probes on the track slab to capture the velocity distribution beneath a moving train. Their findings revealed higher flow speeds beneath the front bogie compared with the rear ones owing to boundary layer growth beneath the train floor. To simulate this, they adjusted the velocity profile in a wind tunnel beneath a one-seventh scale model train to match that of an operational train.

Also in a wind tunnel test, Latorre Iglesias *et al.*<sup>9</sup> investigated the aerodynamic noise generated by motor and trailer bogies at one-seventh scale. They found that both configurations exhibited similar noise spectra, which can be attributed to nearly identical components exposed to the incoming flow, while internal components shielded by the bogie cavity contributed less to the overall noise. Similarly, Sawamura *et al.*<sup>10</sup> conducted experiments using a one-seventh scale model in a wind tunnel, positioning a two-dimensional (2D) microphone array beneath the bogie to identify source regions. They found primary noise sources at low frequencies toward the rear of the bogie. Yamazaki *et al.*<sup>11</sup> installed a 2D microphone array at the trackside using another one-seventh scale model in a wind tunnel, and estimated noise contributions from components inside the bogie cavity by arranging various components within it. Despite revealing phenomena and characteristics of bogie noise generation, experimental results have not fully revealed the underlying mechanisms, necessitating numerical simulations to address these limitations.

Simulating bogie aerodynamics, especially aeroacoustics, presents significant challenges due to the complex geometry and complicated flow phenomena. When choosing a simulation approach, it is crucial to consider the required flow field information, turbulence model requirements, and computational resources. Grid resolution, especially in the boundary layer around the structure, must meet criteria specified by the chosen turbulence models.

Zhang *et al.*<sup>12</sup> and Wang *et al.*<sup>13</sup> utilized the detached eddy simulation (DES) method to investigate the influence of the shape of the bogie and its cavity on the surrounding flow structure and the aerodynamic performance of a high-speed train. Liang *et al.*<sup>14</sup> studied the characteristics of the aerodynamic noise of the leading car of a high-speed train using large eddy simulation and the Ffowcs Williams–Hawkins (FW-H) analogy. Although several numerical investigations have explored whole train models incorporating bogies,<sup>12–19</sup> most have focused on the overall flow field without providing detailed grid information or flow characterization of the bogie region. Discretizing a bogie with complex geometry for computational fluid dynamics (CFD) simulations appears to be a bottleneck, prompting the simplification of bogie geometry as an alternative. In a step toward modeling a simplified bogie, Zhu *et al.*<sup>20</sup> simulated an isolated wheelset of a high-speed train at one-tenth scale, revealing tonal noise due to vortex shedding from both the axle and wheel. Subsequently, the model was expanded to include tandem wheelsets before progressing to a simplified bogie configuration with tandem wheelsets linked via a highly simplified bogie frame composed of two parallel square bars. Finally, the simplified bogie was placed in a cavity.<sup>21–23</sup> Once the model was installed in the cavity of the bogie, the tonal vortex shedding was largely suppressed and the noise became broadband. Subsequently, Li *et al.*<sup>24</sup> placed the simplified bogie under a simplified car body to study the noise generation mechanisms of a leading car.

As mentioned above, there are two crucial issues associated with these numerical simulations. In some studies, the boundary layer grid, which is critical for accurate flow separation assessments,<sup>25–27</sup> lacks sufficient refinement. In others, the bogie geometry lacks details. Thus, there is an urgent need to explore a practical approach that combines a sufficiently fine yet affordable CFD grid for discretizing the bogie with realistic geometry, including all main components and features.

In three-dimensional (3D) CFD models, structured, unstructured, and hybrid grids are commonly used for discretization. Structured grids, aligned with the flow, enhance accuracy and convergence, but are difficult to generate for complex geometries.<sup>22,28–30</sup> Unstructured grids, using tetrahedral or polyhedral cells, offer flexibility and can be generated automatically. Polyhedral grids have advantages such as better gradient approximation and reduced computational resource requirements compared with tetrahedral grids.<sup>29,31–33</sup> A hybrid grid, combining structured and unstructured grids, has been successful in various applications,<sup>34–36</sup> but has not been widely applied to train bogies.

In this study, a practical numerical approach is developed to predict the aerodynamic noise generated by a high-speed train bogie. It involves scaling and constructing the bogie model, generating a hybrid grid, simulating flow fields and acoustic radiation, and scaling the acoustic results. In most studies using conventional hybrid grids,<sup>34–36</sup> both the structured and unstructured grids may exist in both the boundary layer region and the far-field volume, since these are generated automatically by the commercial software. However, the mesh quality, especially in the boundary layer region, cannot be ensured in models with complex geometries. Unlike these conventional hybrid grids, in the present work, a fully structured hexahedral grid is established near the model surfaces, while an unstructured polyhedral grid fills the rest of the volume. This ensures that the quality of the boundary layer grid is guaranteed, while the unstructured grid in the volume retains its flexibility. The methodology for generating this hybrid grid is explored. Additionally, the flow field around the bogie and the noise generation mechanism are investigated, providing insight into bogie noise generation for future numerical studies.

## II. MODEL GEOMETRY AND NUMERICAL SETTINGS

The bogie model depicted in Fig. 1 retains all major components to ensure a realistic bogie geometry, including wheelsets, motors, gearboxes, axle boxes, dampers, air springs, frame, and bolster. However, minor features are simplified; for example, the wheels are represented by disks, neglecting the flange and the smaller thickness in the wheel web region. Similar simplifications are applied to axles, motors, gearboxes, and damper end plates. Components beneath the bolster beam, such as the traction block and lateral dampers, are substituted with a single block with equivalent blockage ratio.

The primary aim of this research is to explore the utilization of a hybrid grid system to facilitate affordable numerical simulations for flow around a bogie with complex geometry. To simplify computations, the influence of the train nose on incoming flow is neglected and the bogie is placed in a simplified cavity, as shown in Fig. 2.

To minimize computational cost, the speed of the flow is set to 10 m/s and the bogie model is downscaled to a 1:12 scale, resulting

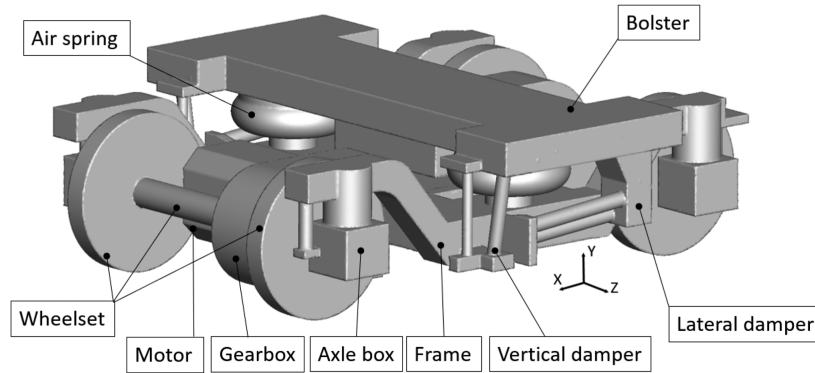


FIG. 1. 3D model of bogie.

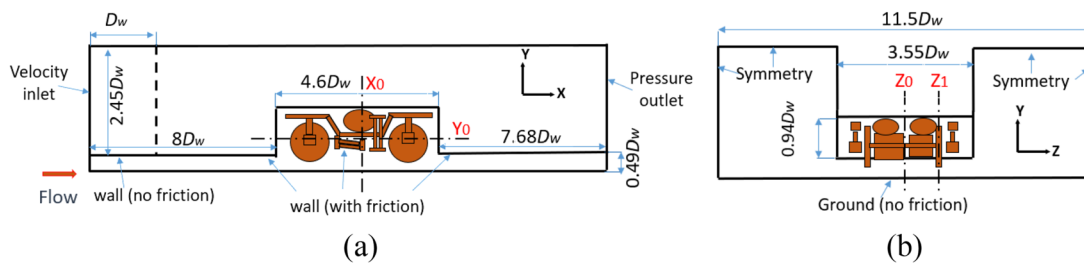


FIG. 2. Sketches of bogie in a simplified cavity (not to scale): (a) side view; (b) end view.  $D_w$  is the wheel diameter.

in a Reynolds number  $UD/\nu$  (where  $U$  is the freestream velocity,  $D$  is a typical dimension, and  $\nu$  is the molecular viscosity) of  $1.91 \times 10^5$  based on the width of the car body  $W_0$  (0.287 m). This falls within the Reynolds number range investigated by Lauterbach *et al.*,<sup>5</sup> who observed that the noise produced by the front bogie exhibited only a weak dependence on the Reynolds number in the range  $1.53 \times 10^5$  to  $3.7 \times 10^6$ . The coordinates of the train are adopted, in which the train remains stationary, while the ground and the incoming flow move in the opposite direction at the operational speed of the train. The coordinate origin is situated at the center of the bogie, aligned with the midplane and positioned at the same level as the centers of the wheels.

Figure 2 also shows the boundary conditions used in the simulations. Ground friction effects are neglected, and so a free-slip boundary condition is applied to the ground. Top and side domain boundaries are set as symmetry. A constant velocity (10 m/s) is applied at the inlet, and a pressure outlet boundary condition is used at the outlet with zero gauge pressure. The inlet extends  $8D_w$  upstream, where  $D_w$  is the diameter of the wheels. To stabilize the simulation, a free-slip wall is used over a length of  $D_w$  after the inlet, with a no-slip wall over the remaining length of  $7D_w$ . The downstream length is set to  $7.68D_w$ , and the lateral domain size to  $11.5D_w$ . These are carefully selected to ensure that the downstream outlet and side boundary conditions do not affect the flow in the bogie region. The distance between the simplified car body bottom and ground is  $\sim 0.49D_w$ . A gap of 250 mm ( $0.33D_w$ ) is maintained between the ground and the bottom of the wheels.

Considering that the Mach number is less than 0.3, the solution to the incompressible 3D unsteady Navier–Stokes equations is obtained, using delayed DES (DDES) with the Spalart–Allmaras (S–A) turbulence model.<sup>37,38</sup> Prior to the unsteady simulation using DDES, a Reynolds-averaged Navier–Stokes (RANS) simulation employing the S–A turbulence model is performed to establish the initial flow field.

### III. HYBRID GRID GENERATION AND VALIDATION

Predicting aerodynamic noise requires a high-quality computational grid, because the signals relevant to the noise are only a small portion of the turbulence and are susceptible to numerical errors.<sup>39</sup> The hybrid grid is generated by first creating a high-quality structured grid with hexahedral cells near solid surfaces using ANSYS IcemCFD 14.1. Next, an unstructured tetrahedral grid is created for the remaining domain and merged with the hexahedral grid at an interface region. Finally, using ANSYS Fluent 14.8, the tetrahedral grid is converted to a polyhedral grid, which is less sensitive to stretching<sup>31</sup> and contains a smaller number of cells than the tetrahedral one.

#### A. Validation of hybrid grid strategy

Before meshing the bogie shown in Fig. 1, simulations are conducted of flow over circular and approximately square cylinders to validate the hybrid grid generation procedure and establish appropriate numerical settings. The Reynolds number is  $10^5$  for the



circular cylinder (based on the cylinder diameter  $D = 0.05$  m) and  $8.2 \times 10^4$  for the square one (based on the side width of the square cylinder  $D = 0.041$  m).

Comparisons are made between two types of grid for discretizing the flow over circular and square cylinders. Grid type I corresponds to a structured grid from Liu,<sup>40</sup> with all grid parameters similar to those utilized in that study. Grid type II employs a hybrid approach, utilizing the same near-wall structured grid parameters and a polyhedral grid for the rest of the domain. Cases c-I and c-II represent the circular cylinder with grid types I and II, while s-I and s-II represent the square cylinder with grid types I and II. Figure 3 displays the hybrid grid (type II) distribution near the cylinders.

Identical to that in the studies by Liu,<sup>40</sup> the computational domain of the circular cylinder is  $30D \times 20D \times 3D$ , while that for the square cylinder case is  $30D \times 20D \times 4D$ . The cylinder center is positioned  $10D$  from the inlet boundary. The boundary conditions for the circular and square cylinder cases can be found in Refs. 41 and 42, respectively. There are  $2.5 \times 10^6$  cells for case c-I,  $1.86 \times 10^6$  for case c-II,  $2.2 \times 10^6$  for case s-I, and  $1.47 \times 10^6$  for case s-II.

Table I lists various parameters summarizing the flow for the circular cylinder:  $C_d = F_{drag}/(0.5\rho U_\infty^2 DL)$  is the mean drag coefficient, where  $F_{drag}$  is the drag force,  $\rho$  is the density of air,  $U_\infty$  is the freestream velocity (30 m/s),  $D$  is the cylinder diameter and  $L$  is its length;  $C_{l,rms} = F_{lift}/(0.5\rho U_\infty^2 DL)$  is the root-mean-square (rms) value of the lift coefficient, where  $F_{lift}$  is the lift force; and  $St = fD/U_\infty$  is the Strouhal number corresponding to the frequency  $f$  of vortex shedding. The flow separates from the cylinder at an angle  $\theta_{SEP}$  measured from the front stagnation point.

Table I shows that deviations between the present results and published data are within 6%, except for  $C_{l,rms}$ , which is sensitive to simulation and experimental conditions. Comparing the results of case c-I and case c-II, it can be seen that the differences in the mean drag coefficient  $C_d$  and separation angle  $\theta_{SEP}$  are less than 1%, while the differences in  $St$  and  $C_{l,rms}$  are under 2.5%. This indicates that comparable performance is achieved by hybrid and structured grids.

In Table II, the differences in  $C_d$  and  $C_{d,rms}$  between case s-I and the results of Liu<sup>40</sup> are ~14% and that for  $C_{l,rms}$  is about 7%. The simulated results from Liu<sup>40</sup> were for a cylinder of radius 0.5 mm with rounded corners, with a finely tuned grid being used near these corners, which improves alignment with the experimental data. The results of s-I and s-II are very close to each other. Computations are

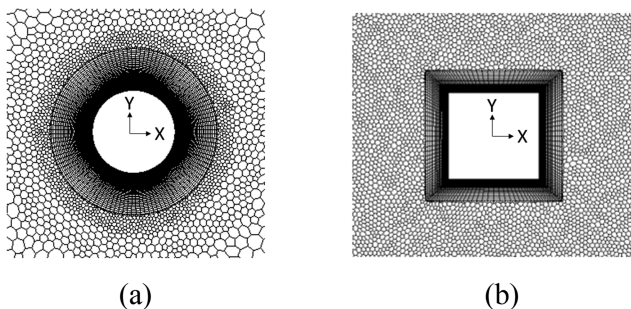


**FIG. 3.** Details of the hybrid grid system used for cylinder flow: (a) hybrid grid around circular cylinder (case c-II); (b) hybrid grid around square cylinder (case s-II).

**TABLE I.** Comparison of results for circular cylinder at  $Re = 10^5$ .

Grid type	Case	$C_d$	$C_{l,rms}$	$St$	$\theta_{SEP}$ (deg)
Structured	c-I	1.16	0.580	0.185	82.0
Hybrid	c-II	1.17	0.563	0.192	82.5
Num.	Liu <sup>40</sup>	1.23	0.73	0.19	84.0
Expt.	Schewe <sup>43</sup>	1.21	0.29	0.20	...
Expt.	Norberg <sup>44</sup>	...	0.51	0.19	...
Error (%)	Error of c-I	5.7	20.5	2.6	2.3
	Error of c-II	4.9	22.8	1.0	1.9

**TABLE II.** Comparison of results for square cylinder at  $Re = 8.2 \times 10^4$ .

Grid type	Case	$C_d$	$C_{d,rms}$	$C_{l,rms}$	$St$
Structured	s-I	2.39	0.238	1.48	0.130
Hybrid	s-II	2.38	0.195	1.47	0.130
Hybrid	s-IIa	2.06	0.199	1.39	0.128
Num.	Liu <sup>40</sup>	2.08	0.210	1.38	0.129
Expt.	Vickery <sup>45</sup>	2.05	0.170	1.30	0.120
Expt.	Norberg <sup>46</sup>	2.10	...	...	0.130
Error (%)	Error of s-I	14.9	13.3	7.2	0.8
	Error of s-II	14.9	15.2	7.2	0.8
	Error of s-IIa	1	5.2	0.7	0.8

also performed for a hybrid grid case with rounded corners (s-IIa), utilizing grid parameters similar to those of case s-II. The results for case s-IIa show closer agreement with both the experimental data and numerical results from Liu<sup>40</sup> than the other two cases featuring sharp corners. However, to simplify grid generation for subsequent bogie component simulations, rounded corners will not be used.

Pressure data sampled on the square cylinder surface are input into the FW-H equation to compute far-field noise,<sup>47</sup> with receivers positioned at the cylinder midspan, 5 m radially from the axis. Figure 4 shows the one-third octave band spectrum of the sound pressure level (SPL) and the angular distribution of the overall sound pressure level (OASPL) computed using the hybrid grid. These results are compared with the numerical and experimental results of Liu.<sup>40</sup> The experimental data have been rescaled to match the numerical conditions. Figure 4(a) shows the noise spectra corresponding to a receiver positioned perpendicular to the flow direction, i.e., at  $\theta = 90^\circ$ . Good agreement is found between the peaks. Figure 4(b) plots the overall level against angle. The present results are slightly higher than the numerical result from Liu,<sup>40</sup> with a maximum deviation of ~1 dB.

## B. Hybrid grid generation for bogie model

To create the hexahedral boundary layer grid for the bogie, the bogie is segmented into five distinct parts on the basis of their geometric attributes, as illustrated in Fig. 5(a)–5(e). Different surface grid sizes are specified for these five parts according to the local flow

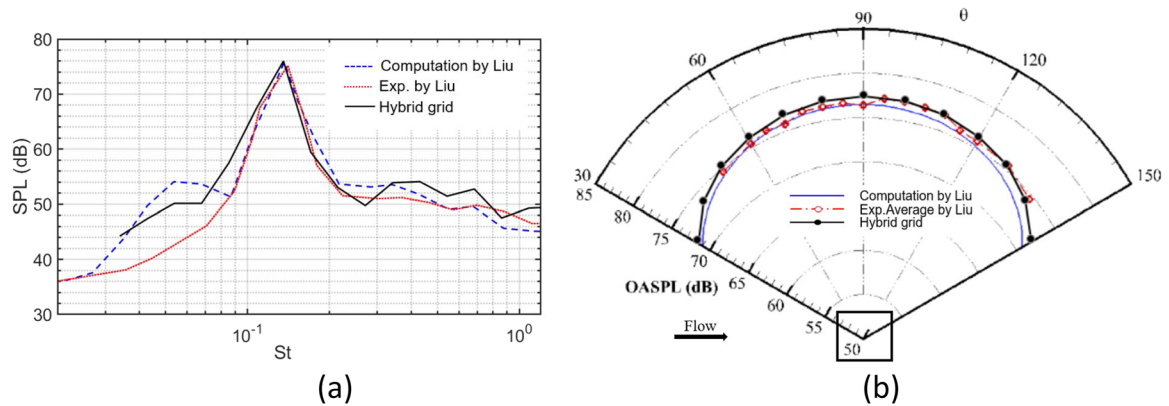


**FIG. 4.** Aerodynamic noise of the square cylinder at  $Re = 8.2 \times 10^4$ : (a) noise spectra at  $90^\circ$  (one-third octave); (b) directivity. The experimental data from Liu<sup>40</sup> are scaled to correspond to the numerical conditions.

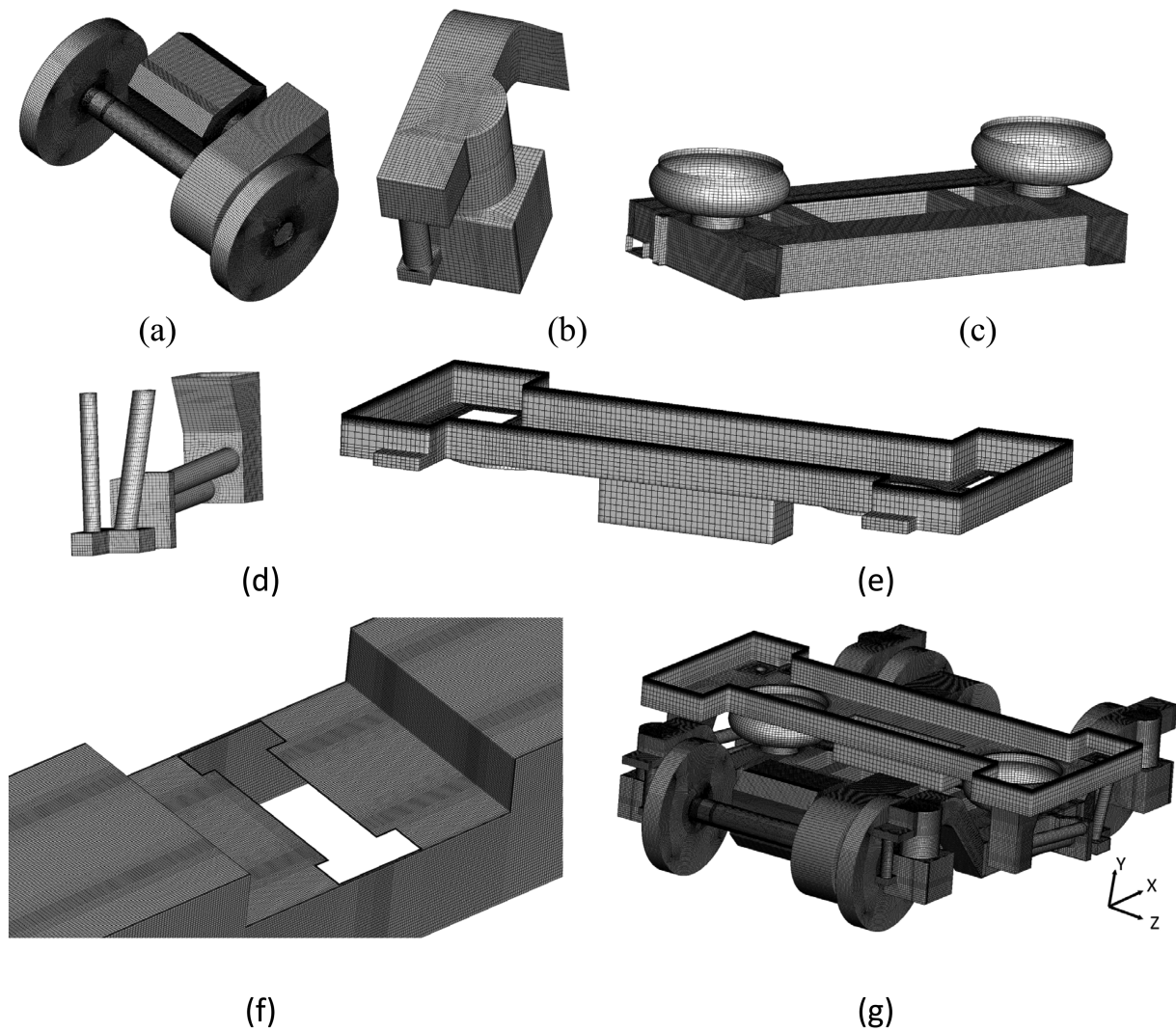


**FIG. 5.** Surface mesh distribution of model components: (a) wheelset (including motor and gearbox); (b) axle box; (c) frame components; (d) side yaw dampers; (e) bolster beam; (f) cavity; (g) whole bogie.

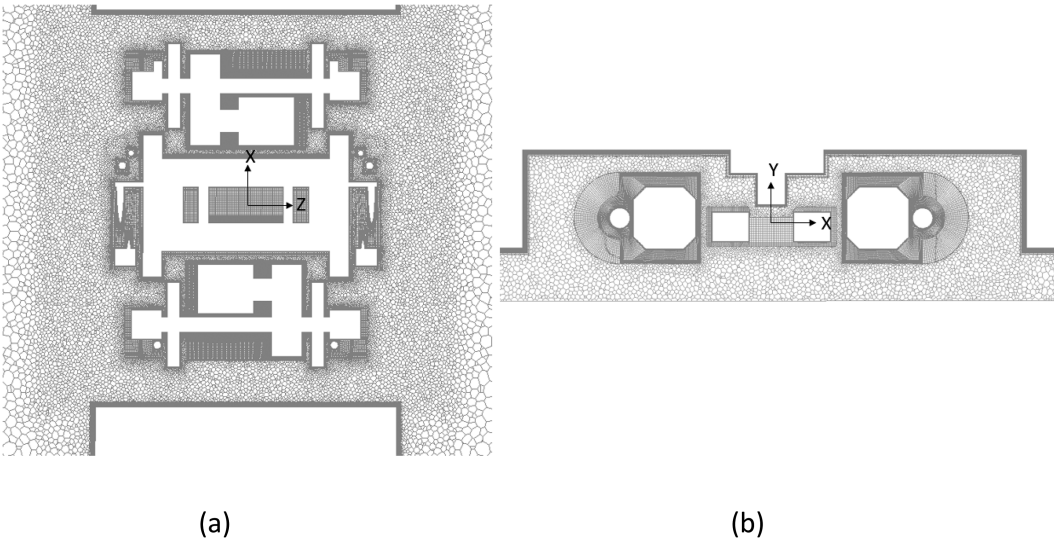


FIG. 6. Mesh distribution on solid surface at the slices defined in Fig. 2: (a) slice  $Y_0$ ; (b) slice  $Z_0$ .

conditions. The boundary layer grid is generated using hexahedral grid generation blocks covering the solid surface in ANSYS Icem-CFD 14.1. The parameters of the boundary layer will be presented in the grid sensitivity study in Sec. III C. After the hexahedral grid has been generated, a tetrahedral grid is used to fill the remaining volume of the computational domain. The volume grid in the cavity is refined with a grid refinement region. Once the hexahedral and tetrahedral grids have been connected, ANSYS Fluent 14.1 is used to convert the tetrahedral grid into a polyhedral grid, reducing the number of cells by half and improving grid quality.<sup>31</sup>

Different slices, denoted by the dash-dotted lines in Fig. 2, are used to illustrate the grid. Figure 6 displays the grid distribution on the slices  $Z_0$  and  $Y_0$ . In the boundary layer, to ensure high resolution, the grid is designed with the highest density in the structured grid near the solid surfaces. As can be seen in Fig. 6(a), the density of the

volume grid is chosen to be greater around the bogie than in other areas because the velocity has greater variation in this region.

C. Grid sensitivity study

To establish an appropriate grid resolution for the bogie model shown in Fig. 1, a grid sensitivity study is performed for a simpler model. This model omits some components (the bolster, motors, and gearboxes) and modifies the side dampers' end plates to flat plates. Owing to the symmetry of the simplified bogie, a half-width model is used, with boundary conditions identical to those in Fig. 2, except that the middle plane is designated as a symmetry boundary condition.

Table III presents details of the grid for the four cases established for the grid study. In the boundary layer region, the

TABLE III. Summary of main grid information.

Components	Parts	Fine	Medium-1	Medium-2	Coarse
Maximum aspect ratio					
Drive system	Wheelset	56	80		112
Bearing component	Axle box	48	65		90
	Front damper	80	110		150
Frame component	Frame	90	125		180
	Air springs	55	80		112
Side dampers	Vertical damper	80	112		160
	Lateral damper	90	128		176
Cavity		105	148	200	210
Total number of cells (million)		18.1	9.6	8.1	4.8



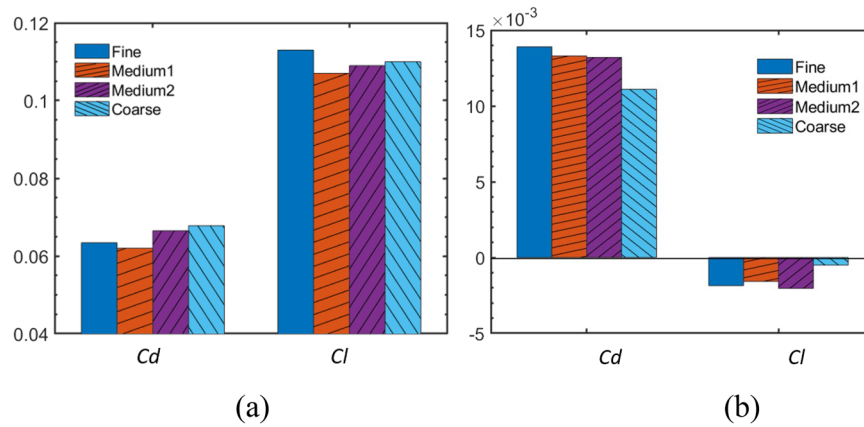


FIG. 7. Summary of force coefficients from different cases: (a) cavity; (b) bogie.

parameters of the hexahedral grid remain constant perpendicular to the wall, while the grid sizes in the other two directions are refined by adjusting the aspect ratio. The nondimensional height of the first cell ( $y^+$ ) on all solid walls is kept below 1. The boundary layer grid consists of 25 layers with an expansion ratio of 1.1. Case medium-2 is created to evaluate the grid aspect ratio within the cavity, differing from case medium-1 only in the grid size in the cavity region. The volume grid in the area around the bogie, where intense turbulent flow is expected, is refined progressively at a ratio of 1.4 between the

coarse, medium, and fine cases. To mitigate the impact of the time step size, the maximum Courant–Friedrichs–Lewy (CFL) value for all calculations is kept below 5. A detailed time-step sensitivity study can be found in Ref. 48.

Figure 7 illustrates the time-averaged drag and lift force coefficients for both the bogie and the cavity, using the full cross-sectional area of the train ( $0.0826 \text{ m}^2$  in the 1/12th scale model) as the reference area. The medium-1 and medium-2 cases show mean values within 5% of the fine case, while the coarse case has more

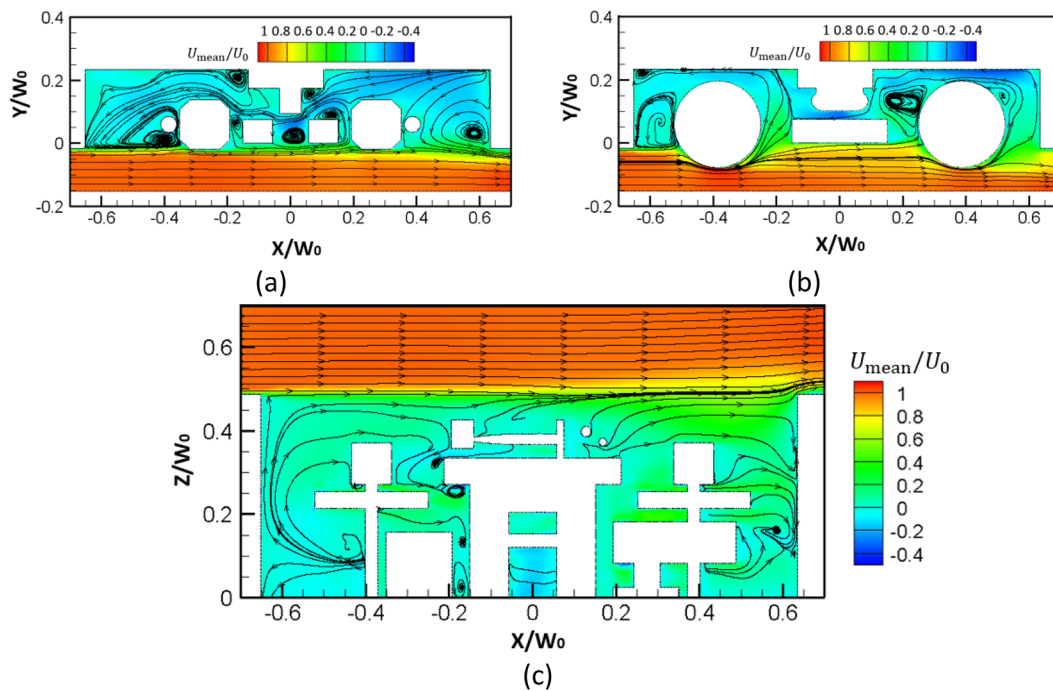


FIG. 8. Contours of time-averaged streamwise velocity alongside 2D mean streamlines: (a) slice  $Z_0$ ; (b) slice  $Z_1$ ; (c) slice  $Y_0$  (half-width is shown).  $W_0$  is the width of the cavity.

pronounced deviations, except for the lift coefficient of the cavity. Therefore, the grid parameters of medium-1 and medium-2 are more suitable than those of the coarse case. For the full bogie model discretization, the medium-1 grid parameters are preferred. However, owing to the complexity in the vicinity of the bogie bolster beam, as shown in Fig. 5(e), adjustments are made to enhance local mesh quality, resulting in actual mesh sizes within the cavity varying between the medium-1 and medium-2 cases.

#### IV. NUMERICAL RESULTS AND DISCUSSION

The grid parameters chosen in Sec. III C are implemented in the subsequent simulations for the full bogie and cavity model depicted in Figs. 1 and 2. Based on these grid parameters, the full model has about  $23.8 \times 10^6$  cells. A time step size of  $1.5 \times 10^{-5}$  s is selected to ensure that the maximum CFL remains smaller than 5. The total simulation time is  $\sim 5.6$  s, which corresponds to 36 flow-through times of the computational domain. The wall-time of the simulation is around 1120 h when employing 512 processors on the Iridis4 high performance computer at the University of Southampton.

##### A. Aerodynamic results

To investigate the noise generation mechanism, analyses are conducted on the time-averaged velocity field, instantaneous vorticity fields, and wall pressure fluctuations. Figure 8 presents contours of the mean streamwise velocity across three slices (as indicated in

Fig. 2), overlaid with 2D mean streamlines. In general, the flow predominantly enters the cavity from the bottom. Within the bogie cavity, the flow exhibits a notably lower velocity, recirculating gradually from the rear to the front through the upper section of the cavity. Moreover, the bottom and sides of the bogie are exposed to higher-speed flows than the components inside the cavity.

Figure 9 displays the contours of the instantaneous vorticity  $\Omega$  across the same three slices. It can be observed that the shear flow detaches from the cavity leading edge, a phenomenon consistent with findings in the simulations conducted by Zhu *et al.*<sup>22</sup> This flow then impinges on the lower sections of the cavity trailing edge and the bogie. However, in contrast to the results of Zhu *et al.*,<sup>22</sup> after detaching from the upstream cavity edge, the shear layer does not bend and penetrate into the cavity. Instead, it travels downstream and interacts with certain components, such as the side dampers and the bottom of the bogie. This disparity with the results of Zhu *et al.*<sup>22</sup> can be largely attributed to the differences in geometrical configurations, such as the presence of additional components in the cavity, the different height of the floor above the ground, and the greater blockage ratio of the shielded part of the bogie. Subsequently, the interaction with the bogie causes the detached shear layer to disperse in the downstream direction, leading to a portion of it impacting the rear surface of the cavity. Morris<sup>49</sup> noted that in shallow open cavities, the dipole noise is produced by the unsteady pressure fluctuations on the cavity surface caused by the detached shear layer. This principle similarly applies to the model depicted in Fig. 2. The pressure fluctuations resulting from the interaction

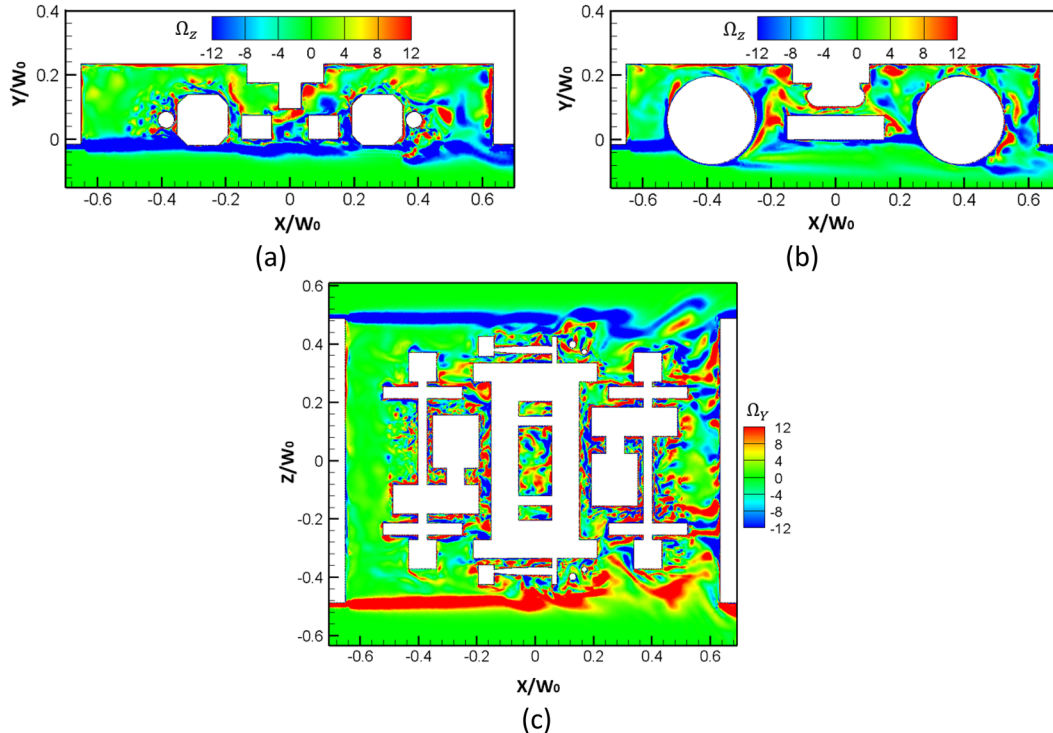


FIG. 9. Contours of instantaneous vorticity field: (a)  $\Omega_z$  on slice  $Z_0$ ; (b)  $\Omega_z$  on slice  $Z_1$ ; (c)  $\Omega_y$  on slice  $Y_0$ .  $W_0$  is the cavity width.

between the detached shear layer and the solid surfaces of the model could serve as potential sources of the dipole noise.

In Fig. 10, the vortex structures are visualized by isosurface of the nondimensional quantity  $\bar{Q} = Q/(U_0/W_0)^2$  and colored by the velocity ratio  $U_{\text{mag}}/U_0$ . Here,  $Q$  is the second invariant of the velocity gradient,  $U_{\text{mag}}$  is the local instantaneous velocity magnitude,  $U_0$  is the freestream velocity, and  $W_0$  is the width of the train body (0.287 m in scaled size). The isosurface is plotted for  $\bar{Q} = 3$ . It can be noted that the sides and bottom of the bogie are covered by vortices shed from the upstream rim of the cavity. This vortical flow interacts with the bottom and side components until it is hindered by the rear surface of the cavity. Areas impacted or flushed by the vortical flow have high surface pressure fluctuations, which, in turn, could generate aerodynamic noise.

To establish a connection between the flow behavior and aerodynamic noise sources, the distribution of the pressure fluctuations on the solid surfaces is investigated. The rms value of the rate of change of pressure,  $dp/dt$ , on the solid walls serves as an indicator of dipole noise sources. Its magnitude can be employed to quantify the noise source intensity.<sup>50</sup> To obtain the value over a specific frequency range, this is calculated in decibels as

$$L_p = 10 \log_{10} \left( \sum_{i=1}^n \text{PSD}_i \times df \right), \quad (1)$$

where  $\text{PSD}_i$  is the signal power spectral density of  $dp/dt$  at the  $i$ th frequency,  $df$  is the frequency interval, and  $n$  is the number of frequencies considered, which is set to correspond to the range from 20 to 1000 Hz.

To quantify the strength of the total noise source of a component, the power of every surface element of the component is summed:

$$L_{p\_total} = 10 \log_{10} \left\{ \sum_{j=1}^m \left[ \sum_{i=1}^n (\text{PSD}_{ij} \times df) \times dA_j \right] \right\}, \quad (2)$$

where  $m$  is the total number of grid elements associated with the component, and  $dA_j$  is the area of the  $j$ th grid element.

During the simulation, the pressure signals from the surface grid elements are collected (totaling  $\sim 1.12 \times 10^6$ ) over a duration of  $\sim 5$  s. The PSD of each surface element is calculated using Welch's method with a Hanning window. The signal is divided into 25 segments with a 50% overlap and a segment length of 0.4 s, resulting in a frequency resolution of 2.5 Hz. Figure 11 displays the distribution of  $L_p$  on the model surfaces.

Figure 11(a) plots the noise source distribution on the surfaces of the whole model. In general, the strength of  $L_p$  is more significant on the bottom surfaces, particularly at the rear section of both the cavity and the bogie. This observation agrees well with the findings of Sawamura *et al.*,<sup>10</sup> who similarly noted that the most prominent sound sources are situated at the rear portion of the bogie. On the basis of the observations in Figs. 8 and 9, it is found that the detached shear layer impinges on the front part of the bogie, while a wake with strong turbulence impinges on the rear components, resulting in strong noise sources at the rear, as can be seen in Fig. 11(b). Figure 11(c) displays the distribution of  $L_p$  on the cavity surface. A prominent noise source is evident at the rear wall of the cavity, particularly at its corners and along the edges of the bottom surface. Besides the detached shear layer originating from the upstream edge of the cavity, these areas of significant pressure fluctuations are also influenced by the incoming wake flow from upstream. Figure 8(a) illustrates how the rear wall of the cavity allows some of the upstream wake to infiltrate into the cavity. Consequently, as shown in Fig. 11(b) and 11(c), the area of strong noise sources

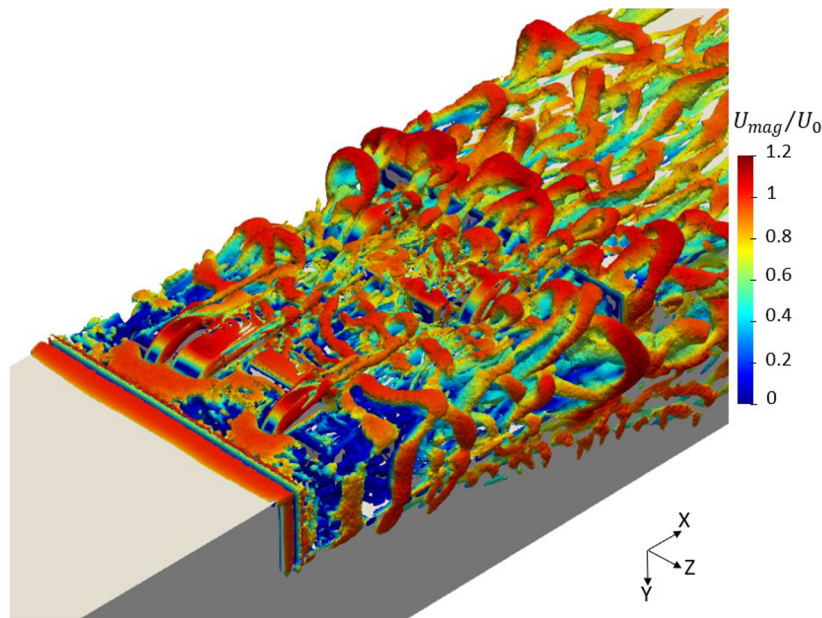
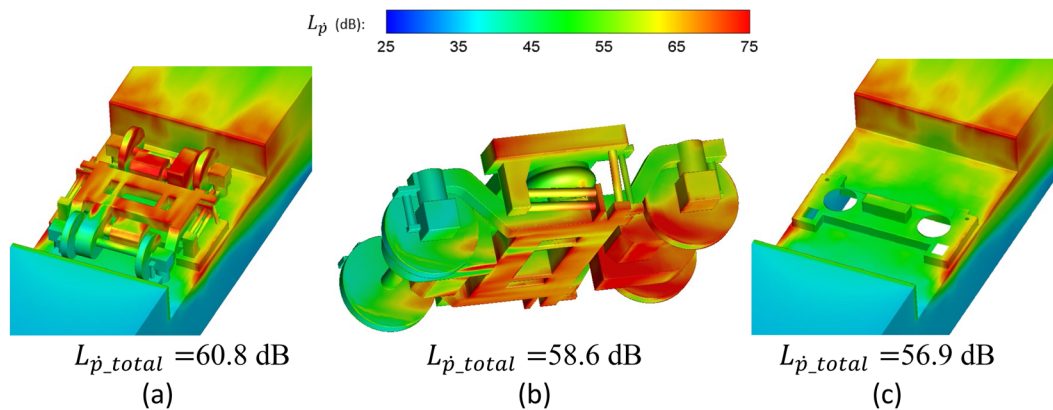


FIG. 10. Vortex structures represented by  $Q/(U_0/W_0)^2$  at a value of 3, colored by  $U/U_0$ .





**FIG. 11.** Contours of the rate of change of pressure,  $dp/dt$ , on the components, integrated from 20 to 1600 Hz: (a) bottom view of the whole model; (b) bogie; (c) bottom view of the cavity.

extends to the upper part of both the cavity and the bogie. The overall level of the rate of change of pressure  $L_{\dot{p}_{total}}$ , as given by Eq. (2), is 2.3 dB higher on the bogie surface than on the cavity surface. However, it is important to note that when calculating  $L_{\dot{p}_{total}}$ , phase information is not considered. Consequently, the far-field noise level originating from the cavity may not necessarily be lower than that from the bogie. This is investigated in Sec. IV B.

To investigate the characteristics of noise sources in different frequency regions, Figs. 12–15 display the contours of  $L_{\dot{p}}$  on the cavity and bogie calculated by Eq. (1) for different frequency bands. As mentioned in Sec. I, the noise generated by a bogie is dominated by low frequencies. Therefore, the frequency bands are initially obtained by uniformly dividing the frequencies below 600 Hz. Then, another division for finer resolution is conducted based on the results of the first division. Since the lowest frequency

of interest is 20 Hz, the lower limit of the first bands is specified as 20 Hz.

The pressure fluctuation on the cavity walls in the frequency range 20–200 Hz, shown in Fig. 12(a), has the greatest power and has a noise source distribution similar to that shown in Fig. 11(a). The value of  $L_{\dot{p}_{total}}$  is also larger than in the two higher-frequency ranges. This indicates that for the noise sources distributed on the cavity walls, the pressure fluctuation in 20–200 Hz makes the greatest contribution. To investigate the noise source distribution in this frequency region further, the pressure fluctuation is divided into three smaller segments, as shown in Fig. 13. The results show that the pressure fluctuation in the region 60–120 Hz has a strong noise source. The noise source at the edge of the cavity rear wall is stronger than in other areas, because of the impingement of the shear flow from upstream, as shown in Figs. 9(a) and 9(b).

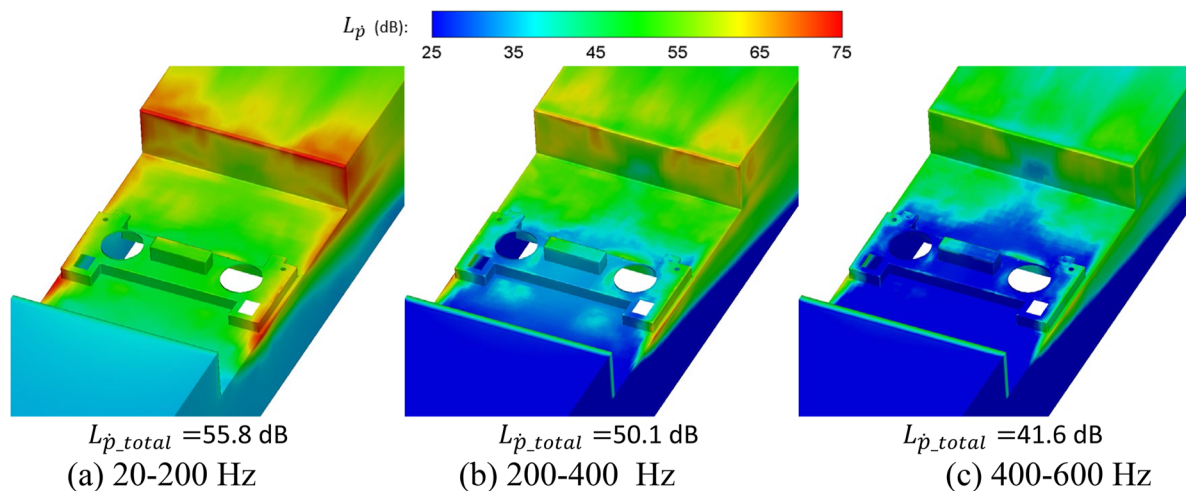


**FIG. 12.** Surface contours of the rate of change of pressure  $dp/dt$  on the cavity (bottom view), integrated over three ranges between 20 and 600 Hz: (a) 20–200 Hz; (b) 200–400 Hz; (c) 400–600 Hz.

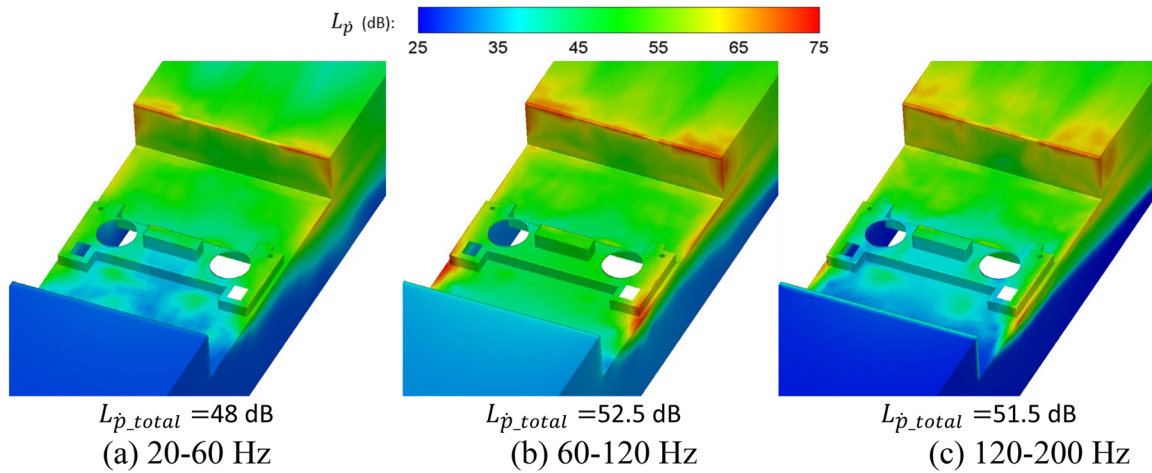


**FIG. 13.** Surface contours of the rate of change of pressure,  $dp/dt$ , on the cavity (bottom view), integrated over three ranges between 20 and 200 Hz: (a) 20–60 Hz; (b) 60–120 Hz; (c) 120–200 Hz.

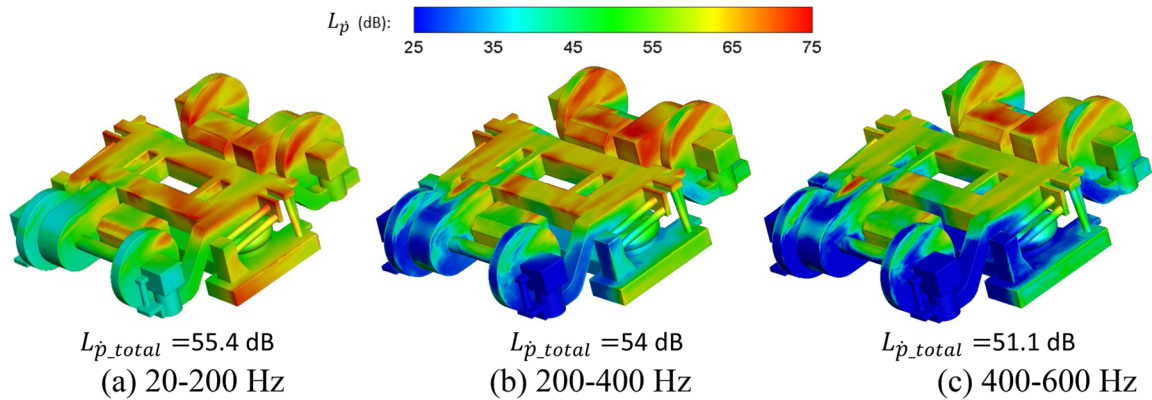


**FIG. 14.** Surface contours of the rate of change of pressure,  $dp/dt$ , on the bogie (bottom view), integrated over three ranges between 20 and 600 Hz: (a) 20–200 Hz; (b) 200–400 Hz; (c) 400–600 Hz.

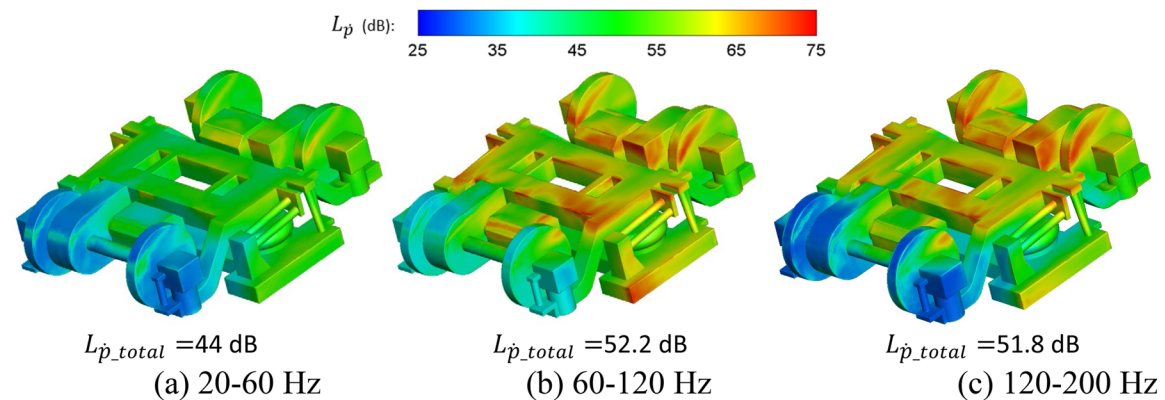


**FIG. 15.** Surface contours of the rate of change of pressure,  $dp/dt$ , on the bogie (bottom view), integrated over three ranges between 20 and 200 Hz: (a) 20–60 Hz; (b) 60–120 Hz; (c) 120–200 Hz.

Figures 14 and 15 depict the corresponding results for the bogie surface. Although the value of the overall noise source strength,  $L_{p\_total}$ , is greatest in the frequency band 20–200 Hz, the strength of the pressure fluctuation on the rear part of the bogie underside is similar to that in the high-frequency bands 200–400 and 400–600 Hz. It is believed that this is because the wake flow from upstream components, shown in Figs. 9(a) and 9(b), has smaller eddies and thus a more uniform energy distribution across the frequency range than that of the detached shear layer from upstream. This also explains the similar distribution of the pressure fluctuation within the smaller frequency range in Figs. 14(b) and 14(c).

From the above analysis of the noise sources in different frequency bands, it can be concluded that the pressure fluctuation makes the greatest contribution from the low frequencies (20–200 Hz) for both the cavity and bogie. This finding is consistent with the experimental studies by Latorre Iglesias *et al.*<sup>9</sup> and Sawamura *et al.*,<sup>10</sup> which also found the noise at low frequencies to be dominant for the bogie region.

## B. Aeroacoustic results

The sampled time-dependent surface pressure data are used as input for the FW–H equation to calculate the far-field noise. The sound pressure level (SPL) obtained from the scaled simulation is converted to the SPL at full scale by adding the following correction:

$$\Delta SPL = 10 \log_{10} \left[ \frac{\left( \frac{D_1}{D_2} \right)^2 \left( \frac{U_1}{U_2} \right)^6}{\left( \frac{r_1}{r_2} \right)^2} \right], \quad (3)$$

where  $D_1/D_2$  is the geometry ratio,  $U_1/U_2$  is the velocity ratio, and  $r_1/r_2$  is the ratio of the receiver distances. Subscripts 1 and 2 denote the full-scale and the scale model situations, respectively. Similarly, the frequency  $f_2$  can be corrected to the full-scale value  $f_1$  by

$$\frac{f_1}{f_2} = \frac{U_1}{U_2} \frac{D_2}{D_1}. \quad (4)$$

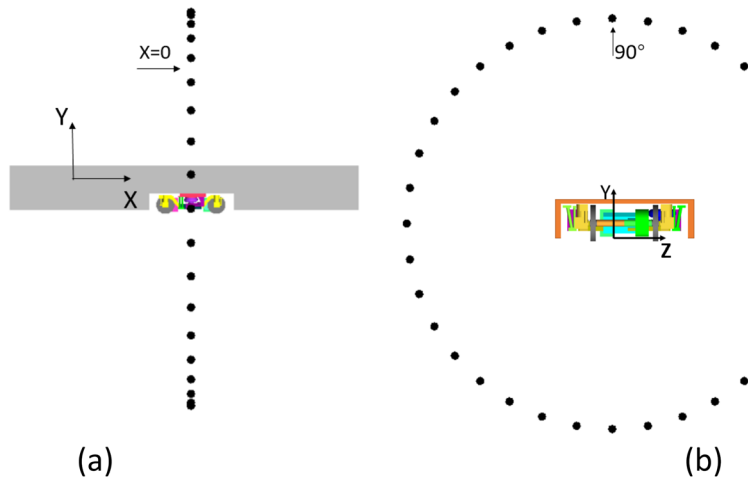


FIG. 16. Sketch of receiver locations: (a) side view; (b) front view.

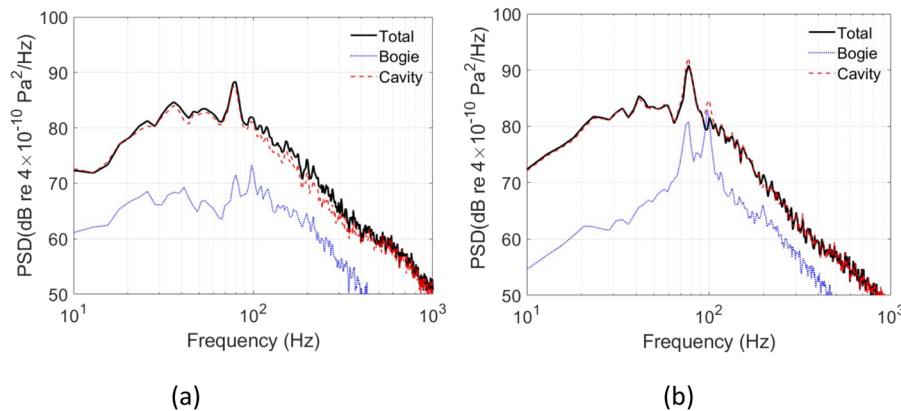


FIG. 17. Noise spectra of the model at the side and top receivers, scaled to the full-scale case at a distance of 20 m distance: (a) side, 0°; (b) top, 90°.

As mentioned earlier, the running speed in the simulations is reduced to 10 m/s, but will be rescaled to 400 km/h, approximately a factor of 11.1, while the dimensions of the bogie model are also scaled down by a factor of 1/12. The distance to the receiver is kept constant. Therefore, to adjust the calculated noise during rescaling, a correction SPL of 84.3 dB is incorporated. Furthermore, according to Eq. (4), the frequency ratio is  $\sim 0.93$  and is applied when scaling the frequencies.

Figure 16 depicts the 36 receivers placed around the bogie. They are evenly distributed, with an angular interval of  $10^\circ$ . The distance between the receivers and the center of the bogie is 20 m, which is greater than the longest acoustic wavelength of interest (17.25 m at 20 Hz) and meets the requirements for the acoustic far field. For the sound propagation, free-field conditions are assumed and acoustic shielding and scattering effects are neglected.

Figure 17 illustrates the noise spectra of the cavity and bogie at the side and top receivers (at  $0^\circ$  and  $90^\circ$ , as shown in Fig. 16). In general, the noise produced by the bogie is significantly lower than that generated by the cavity. In addition, for both the bogie and the cavity, the noise spectra are dominated by frequencies below  $\sim 200$  Hz, which is consistent with the findings from Lauterbach *et al.*<sup>5</sup> and Latorre Iglesias *et al.*<sup>9</sup> On the basis of the above analysis, it can be inferred that the generation of noise at low frequencies is associated with large-scale flow phenomena, such as flow circulation, flapping, and flow recirculation, observed particularly at the rear section of the cavity, as displayed in Figs. 8 and 9. Additionally, both spectra exhibit a minor peak at 78 Hz, with a secondary peak at  $\sim 100$  Hz in the bogie spectrum. These peaks are presumed to be associated with the shear layer detached from upstream and are investigated in more detail below.

Figure 18 presents the directivity of the OASPL generated by both the bogie and the cavity under the assumption of free-field propagation. Although shielding, reflection, and scattering effects are neglected here, this provides an indication of the direction of sound radiation. According to Fig. 18, the noise produced by the

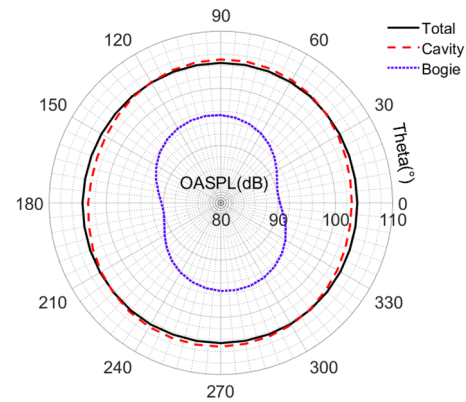
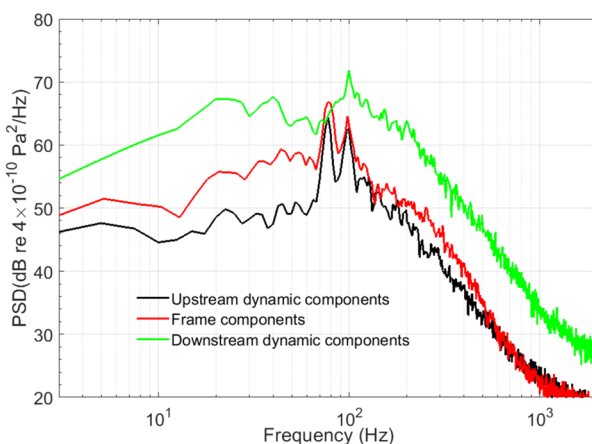


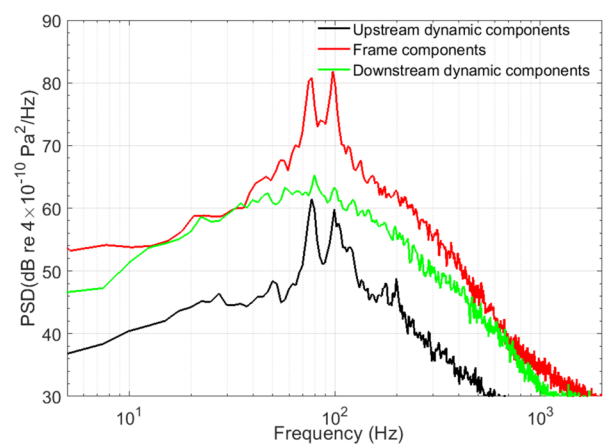
FIG. 18. Far-field noise directivity of the OASPL from the model in a vertical plane, rescaled to the full-scale case at a distance of 20 m.

cavity exceeds that generated by the bogie by a significant margin in all directions. Yamazaki *et al.*<sup>11</sup> and Latorre Iglesias *et al.*<sup>9</sup> also came to this conclusion from experimental observations. However, in their experiments, it was assumed that the flow conditions remained unaffected by the introduction of bogie components into the cavity. Moreover, in reality, the rear corners of the cavity are frequently modified to minimize drag and noise, thus reducing the cavity noise contribution compared with this simplified geometry. The OASPL of the cavity appears to be roughly omnidirectional, whereas the bogie demonstrates stronger radiation in the vertical direction.

To determine the relative contributions of different components, the bogie is partitioned into three groups: the upstream dynamic system, the downstream dynamic system, and the frame system. The dynamic systems encompass the upstream/downstream wheelsets, gearboxes, motors, and axle boxes. The frame group com-



(a)  $0^\circ$



(b)  $90^\circ$

FIG. 19. Sound pressure spectra of the bogie components: (a)  $0^\circ$ ; (b)  $90^\circ$ .



prises components such as the frame, dampers, and air springs. Figure 19 shows the sound pressure spectra due to the three groups of bogie components at the side and top receivers. The noise spectra are calculated from the FW-H equation using sources on the component surfaces within the corresponding group. It is found that the noise levels from the downstream dynamic components are higher at all frequencies. This is consistent with the results given in Figs. 11(a) and 11(b), which show that the rear part of the bogie has greater values of  $L_p$  owing to the impingement of the wake with different size of eddies from upstream components. The noise spectra of the frame components have similar shapes to those of the upstream components. Two peaks are found at frequencies of 78 and 100 Hz.

To identify the flow mechanisms responsible for the peaks, Fig. 20 shows the strength of the pressure fluctuation integrated over frequency bands of 75–85 and 95–105 Hz by Eq. (1). It can be seen that strong pressure fluctuations appear in areas on which the shear layer directly impinges. Two monitors are placed within the area with strong pressure fluctuations, as indicated. Figure 21 depicts the spectra of the pressure coefficients  $C_p$  at these two monitors. Two peaks are also identified, and they have the same frequencies as found in the noise spectra of bogie components given in Fig. 19. They are related to the vortices shed periodically from upstream of the cavity rim.<sup>5</sup> These vortices are then convected downstream as the shear layer propagates with convection and breaks after impinging on the downstream components. The breakdown of these vortices is the reason why the peaks are not as significant in the noise spectra of the downstream dynamic components as they are for the upstream dynamic components.

Figure 22 shows the directivities of the noise from the bogie components. It is worth noting that the dynamic components emit greater OASPLs in the horizontal direction, while the frame components emit larger ones in the vertical direction. Therefore, for the directivity of the bogie, as shown in Fig. 18, the dynamic components contribute more in the lateral direction, while the frame components contribute more in the vertical direction. In addition, the directivity of the frame components is symmetric with respect to the lateral

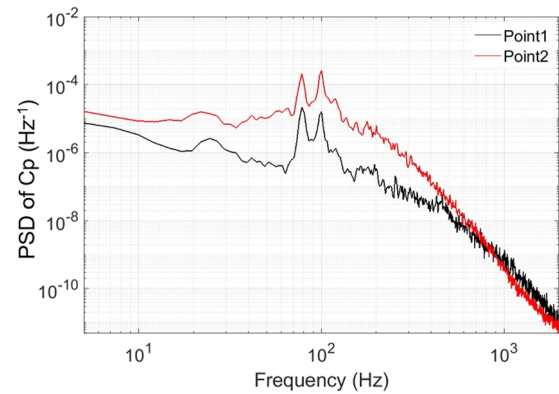


FIG. 21. PSD of  $C_p(t)$  at points 1 and 2 in Fig. 20(b).

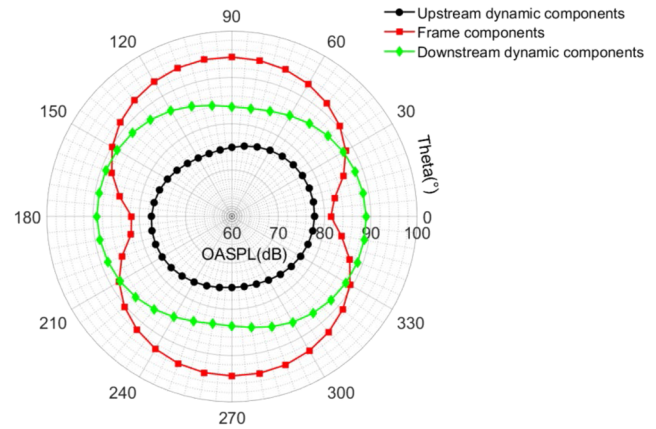


FIG. 22. Noise directivity of the bogie components.

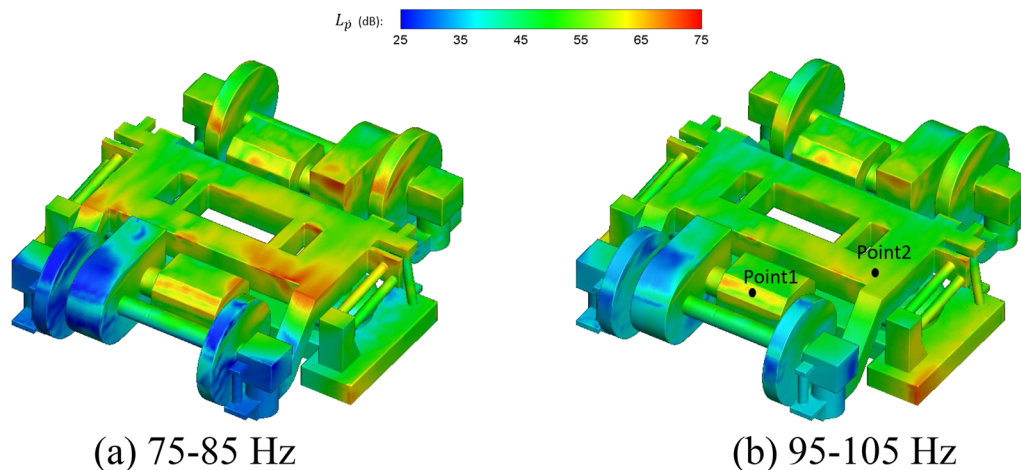


FIG. 20. Surface contours of the rate of change of pressure,  $dp/dt$ , on the bogie (bottom view), integrated around the peak frequencies in Fig. 19: (a) 75–85 Hz; (b) 95–105 Hz.

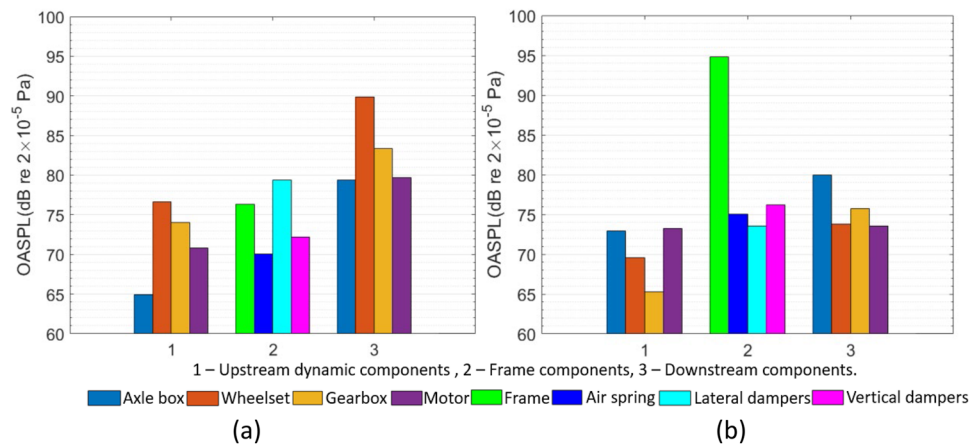


FIG. 23. Noise levels produced by different bogie components at side and top receivers. (a) Side, 0°; (b) top, 90°.

midplane, whereas for the dynamic components it is asymmetric owing to the positions of the motors and gearboxes. Consequently, the directivity of the whole bogie, determined by both the frame components and dynamic components, is slightly oblique to the left, as shown in Fig. 18.

In Fig. 18, the directivity of the cavity is nearly omnidirectional, while the bogie exhibits stronger radiation in the vertical direction. This difference can be attributed to the differences in the noise source distribution on the surfaces of the bogie and the cavity. As shown in Figs. 11(b), 14, and 15, the bottom surfaces of the frame components show strong noise sources covering a larger area than the lateral projected area of the downstream dynamic components, which is also covered by strong noise sources. Consequently, as shown in Fig. 22, the maximum noise level of the frame components is higher in the vertical direction than that of the downstream components in the lateral direction. Thus, the noise directivity of the bogie exhibits higher values in the vertical direction. However, regarding the noise distribution at the rear part of the cavity, as shown in Figs. 11(c), 12, and 13, the vertical and lateral areas with strong noise sources are similar. This balanced distribution results in the directivity of the cavity being close to omnidirectional.

Figure 23 compares the OASPLs at the side and top receivers. This reveals the potential noise contributions of different bogie components: upward to the interior of the car and sideways to the surrounding environment. As shown in Fig. 23(a), among the various bogie components, the wheelsets contribute the most in the lateral direction. This observation is consistent with the experimental results of Yamazaki *et al.*<sup>11</sup> At the side receiver, their noise levels exceed those at the top receiver. As shown in Fig. 11, the values of  $L_p$  are comparable between the wheel rim and the side surfaces of the wheels. However, owing to the larger area of the side surface, the SPL in the lateral direction is larger than that in the upward direction. Similarly, as depicted in Fig. 23(b), also because the bottom of the frame has a larger surface area, the SPL of the frame significantly exceeds that of the other components in the vertical direction.

## V. CONCLUSIONS

A numerical approach has been proposed to analyze the aerodynamic noise generated by a train bogie with realistic geometric features. To discretize the complex bogie model with high-quality and affordable meshes, a hybrid grid system was implemented. This system incorporates a hexahedral grid near the solid surface and a polyhedral grid throughout the remaining volume. Circular and square cylinders were utilized to validate the effectiveness of the hybrid grid concept. Subsequently, a grid sensitivity study was conducted using a half-width model, with the bogie in the model simplified to reduce the computational cost. The chosen grid parameters were then implemented to calculate the noise generated by the complete bogie model within a simplified cavity.

The aerodynamic results reveal that both the shear layer and the turbulent wake from the upstream components contribute to the aerodynamic noise from the bogie. Potential noise source regions are identified as components immersed in either the detached shear layer or the turbulent wake. This is supported by the examination of the distribution of the rate of change of pressure,  $dp/dt$ . The rear section of the bogie and regions around the rear cavity corner show high noise source strengths, owing to the impingement of vortical shear layers and turbulent wakes from upstream components. These results offer valuable insights for future noise reduction measures.

The characteristics of the far-field noise from the bogie and cavity have also been calculated. It is found that the noise level produced by the cavity exceeds that of the bogie, both being dominated by frequencies below ~200 Hz. The low-frequency noise originates mainly from the bottom surfaces of the bogie and the rear wall of the bogie cavity. These findings align with those of experimental studies by Latorre Iglesias *et al.*<sup>9</sup> and Yamazaki *et al.*<sup>11</sup> It is observed that the rear components of the bogie produce higher noise levels than those at the front, a trend consistent with findings reported in the experimental study by Sawamura *et al.*<sup>10</sup>

However, it is important to note some limitations. This study focused only on the bogie, the most complex part, while simplifying the car body to a simple geometry with a cavity. A realistic car



body, for which the hybrid grid method should be well adapted, is necessary to assess its impact on the aerodynamic noise.

## ACKNOWLEDGMENTS

The Ministry of Science and Technology of China has supported the work presented in this paper through the National Key Research and Development Program Grant No. 2016YFE0205200, "Joint Research into Key Technologies for Controlling Noise and Vibration of High-Speed Railways Under Extremely Complicated Conditions." The Iridis4 supercomputer at the University of Southampton facilitated all simulations conducted for this study.

## AUTHOR DECLARATIONS

### Conflict of Interest

The authors have no conflicts to disclose.

### Author Contributions

**Yuan He:** Conceptualization (equal); Data curation (equal); Formal analysis (equal); Methodology (equal); Writing – original draft (equal); Writing – review & editing (equal). **David Thompson:** Conceptualization (equal); Funding acquisition (equal); Project administration (equal); Supervision (equal); Writing – original draft (equal); Writing – review & editing (equal). **Zhiwei Hu:** Conceptualization (equal); Supervision (equal); Writing – original draft (equal); Writing – review & editing (equal).

## DATA AVAILABILITY

No new data were created or analysed in this study. Data sharing is not applicable to this article.

## REFERENCES

- <sup>1</sup>C. Talotte, "Aerodynamic noise: A critical survey," *J. Sound Vib.* **231**(3), 549–562 (2000).
- <sup>2</sup>A. Martens, J. Wedemann, N. Meunier, and A. Leclerc, "High speed train noise-sound source localization at fast passing trains," in *Sociedad Espanola de Acustica*, SEA, 2009.
- <sup>3</sup>K. Nagakura, "Localization of aerodynamic noise sources of Shinkansen trains," *J. Sound Vib.* **293**(3–5), 547–556 (2006).
- <sup>4</sup>D. J. Thompson, E. Latorre Iglesias, X. Liu, J. Zhu, and Z. Hu, "Recent developments in the prediction and control of aerodynamic noise from high-speed trains," *Int. J. Rail Transp.* **3**(3), 119–150 (2015).
- <sup>5</sup>A. Lauterbach, K. Ehrenfried, S. Loose, and C. Wagner, "Microphone array wind tunnel measurements of Reynolds number effects in high-speed train aeroacoustics," *Int. J. Aeroacoustics* **11**(3–4), 411–446 (2012).
- <sup>6</sup>X. Liu, J. Zhang, D. J. Thompson, E. L. Iglesias *et al.*, "Aerodynamic noise of high-speed train pantographs: Comparisons between field measurements and an updated component-based prediction model," *Appl. Acoust.* **175**, 107791 (2021).
- <sup>7</sup>H.-M. Noh, S. Choi, S. Hong, and S.-W. Kim, "Investigation of noise sources in high-speed trains," *Proc. Inst. Mech. Eng., Part F* **228**(3), 307–322 (2014).
- <sup>8</sup>T. Uda, N. Yamazaki, T. Kitagawa, K. Nagakura, and Y. Wakabayashi, "Estimation of aerodynamic bogie noise through field and wind tunnel tests. Noise and vibration mitigation for rail transportation systems," in *Proceedings of the 12th International Workshop on Railway Noise*, 12–16 September 2016 (Springer, Terrigal, Australia, 2018), Vol. 139, pp. 377–387.

- <sup>9</sup>E. Latorre Iglesias, D. J. Thompson, M. Smith, T. Kitagawa, and N. Yamazaki, "Anechoic wind tunnel tests on high-speed train bogie aerodynamic noise," *Int. J. Rail Transp.* **5**(2), 87–109 (2017).
- <sup>10</sup>Y. Sawamura, T. Uda, T. Kitagawa, H. Yokoyama, and A. Iida, "Measurement and reduction of the aerodynamic bogie noise generated by high-speed trains in terms of wind tunnel testing," in *Noise and Vibration Mitigation for Rail Transportation Systems, Notes on Numerical Fluid Mechanics and Multidisciplinary Design*, edited by G. Degrande *et al.* (Springer International Publishing, Cham, 2021), pp. 73–80.
- <sup>11</sup>N. Yamazaki, T. Uda, T. Kitagawa, and Y. Wakabayashi, "Influence of bogie components on aerodynamic bogie noise generated from Shinkansen trains," *Q. Rep. RTRI* **60**(3), 202–207 (2019).
- <sup>12</sup>J. Zhang, J. Wang, Q. Wang, X. Xiong, and G. Gao, "A study of the influence of bogie cut outs' angles on the aerodynamic performance of a high-speed train," *J. Wind Eng. Ind. Aerodyn.* **175**, 153–168 (2018).
- <sup>13</sup>J. Wang, G. Minelli, T. Dong, K. He, and S. Krajnović, "Impact of the bogies and cavities on the aerodynamic behaviour of a high-speed train. An IDDES study," *J. Wind Eng. Ind. Aerodyn.* **207**, 104406 (2020).
- <sup>14</sup>X. F. Liang, H.-F. Liu, T.-Y. Dong, Z.-G. Yang, and X.-M. Tan, "Aerodynamic noise characteristics of high-speed train foremost bogie section," *J. Cent. South Univ.* **27**(6), 1802–1813 (2020).
- <sup>15</sup>J. Lan and J. Han, "Research on the radiation characteristics of aerodynamic noises of a simplified bogie of the high-speed train," *J. Vibroeng.* **19**(3), 2280 (2017).
- <sup>16</sup>J. Mohamed Ali, A. A. Omar, M. B. Ali, and A. R. B. Mohd Baseair, "Numerical investigation of aerodynamic characteristics of high speed train," *IOP Conf. Ser.: Mater. Sci. Eng.* **184**, 012015 (2017).
- <sup>17</sup>C. Zhu, H. Hemida, D. Flynn, C. Baker, X. Liang, and D. Zhou, "Numerical simulation of the slipstream and aeroacoustic field around a high-speed train," *Proc. Inst. Mech. Eng., Part F* **231**(6), 740–756 (2017).
- <sup>18</sup>T. Dong, X. Liang, S. Krajnović, X. Xiong, and W. Zhou, "Effects of simplifying train bogies on surrounding flow and aerodynamic forces," *J. Wind Eng. Ind. Aerodyn.* **191**, 170–182 (2019).
- <sup>19</sup>Z. Guo, T. Liu, Z. Chen, Y. Xia, W. Li, and L. Li, "Aerodynamic influences of bogie's geometric complexity on high-speed trains under crosswind," *J. Wind Eng. Ind. Aerodyn.* **196**, 104053 (2020).
- <sup>20</sup>J. Zhu, Z. Hu, and D. Thompson, "Flow simulation and aerodynamic noise prediction for a high-speed train wheelset," *Int. J. Aeroacoustics* **13**(7–8), 533–552 (2014).
- <sup>21</sup>J. Zhu, Z. Hu, and D. J. Thompson, "Flow behaviour and aeroacoustic characteristics of a simplified high-speed train bogie," *Proc. Inst. Mech. Eng., Part F* **230**(7), 1642–1658 (2016).
- <sup>22</sup>J. Zhu, Z. Hu, and D. Thompson, "The flow and flow-induced noise behaviour of a simplified high-speed train bogie in the cavity with and without a fairing," *Proc. Inst. Mech. Eng., Part F* **232**(3), 759–773 (2018).
- <sup>23</sup>J. Zhu, Z. Hu, and D. Thompson, "The effect of a moving ground on the flow and aerodynamic noise behaviour of a simplified high-speed train bogie," *Int. J. Rail Transp.* **5**(2), 110–125 (2017).
- <sup>24</sup>C. Li, J. Zhu, Z. Hu, Z. Lei, and Y. Zhu, "Investigation on aerodynamic noise generated from the simplified high-speed train leading cars," *Int. J. Aeroacoustics* **21**(3–4), 218–238 (2022).
- <sup>25</sup>P. R. Spalart, "Young person's guide to detached-eddy simulation grids," Tech. Rep. NASA CR-2001-211032 (Langley Research Center, Hampton, VA, 2001).
- <sup>26</sup>P. Spalart and S. Allmaras, "A one-equation turbulence model for aerodynamic flows," in *30th Aerospace Sciences Meeting and Exhibit*, AIAA Paper 1992-0439 (AIAA, 1992).
- <sup>27</sup>M. Shur, P. Spalart, M. Strelets, and A. Travin, "Detached-eddy simulation of an airfoil at high angle of attack," in *Proceedings of the 4th International Symposium on Engineering Turbulence Modelling and Measurements*, Ajaccio, Corsica, France, 24–26 May, 1999 (Elsevier, 1999), pp. 669–678.
- <sup>28</sup>M. M. Hefny and R. Ooka, "CFD analysis of pollutant dispersion around buildings: Effect of cell geometry," *Build. Environ.* **44**(8), 1699–1706 (2009).
- <sup>29</sup>H. Chen, X. Zhou, Z. Feng, and S.-J. Cao, "Application of polyhedral meshing strategy in indoor environment simulation: Model accuracy and computing time," *Indoor Built Environ.* **31**(3), 719–731 (2022).

- <sup>30</sup>R. Duan, W. Liu, L. Xu, Y. Huang *et al.*, "Mesh type and number for the CFD simulations of air distribution in an aircraft cabin," *Numer. Heat Transfer, Part B* **67**(6), 489–506 (2015).
- <sup>31</sup>M. Peric and S. Ferguson, "The advantage of polyhedral meshes," *Dynamics* **24**, 45 (2005).
- <sup>32</sup>Y. Liu, Z. Long, and W. Liu, "A semi-empirical mesh strategy for CFD simulation of indoor airflow," *Indoor Built Environ.* **31**, 1420326X221089825 (2022).
- <sup>33</sup>F. Juretić and A. Gosman, "Error analysis of the finite-volume method with respect to mesh type," *Numer. Heat Transfer, Part B* **57**(6), 414–439 (2010).
- <sup>34</sup>J. Shaw and A. Peace, "Simulating three-dimensional aeronautical flows on mixed block-structured/semi-structured/unstructured meshes," *Int. J. Numer. Methods Fluids* **39**(3), 213–246 (2002).
- <sup>35</sup>L. Tyssel, "Hybrid grid generation for complex 3D geometries," in *Proceedings of the 7th International Conference on Numerical Grid Generation in Computational Field Simulation* (NSF Engineering Research Center for Computational Field Simulation, College of Engineering, Mississippi State University, 2000), pp. 337–346.
- <sup>36</sup>K. Becker, K. Heitkamp, and E. Kügeler, "Recent progress in a hybrid-grid CFD solver for turbomachinery flows," in *Proceedings 5th European Conference on Computational Fluid Dynamics ECCOMAS CFD*, 2010.
- <sup>37</sup>P. R. Spalart, S. Deck, M. L. Shur, K. D. Squires, M. K. Strelets, and A. Travin, "A new version of detached-eddy simulation, resistant to ambiguous grid densities," *Theor. Comput. Fluid Dyn.* **20**(3), 181 (2006).
- <sup>38</sup>P. R. Spalart, "Strategies for turbulence modelling and simulations," *Int. J. Heat Fluid Flow* **21**(3), 252–263 (2000).
- <sup>39</sup>M. Carley, "Turbulence and noise" (2011) Chapter 5: The generation of sound <https://people.bath.ac.uk/ensmjc/Notes/tnoise.pdf>
- <sup>40</sup>X. Liu, "Aerodynamic noise from components of a train pantograph and its reduction," Ph.D. thesis, University of Southampton, 2017.
- <sup>41</sup>X. Liu, D. J. Thompson, and Z. Hu, "Numerical investigation of aerodynamic noise generated by circular cylinders in cross-flow at Reynolds numbers in the upper subcritical and critical regimes," *Int. J. Aeroacoustics* **18**(4–5), 470–495 (2019).
- <sup>42</sup>X. Liu, Z. Hu, D. Thompson, and V. Jurdic, "Reduction of aerodynamic noise from square bars by introducing spanwise waviness," *J. Sound Vib.* **435**, 323–349 (2018).
- <sup>43</sup>G. Schewe, "On the force fluctuations acting on a circular cylinder in cross-flow from subcritical up to transcritical Reynolds numbers," *J. Fluid Mech.* **133**, 265–285 (1983).
- <sup>44</sup>C. Norberg, "Flow around a circular cylinder: Aspects of fluctuating lift," *J. Fluid. Struct.* **15**(3–4), 459–469 (2001).
- <sup>45</sup>B. J. Vickery, "Fluctuating lift and drag on a long cylinder of square cross-section in a smooth and in a turbulent stream," *J. Fluid Mech.* **25**(3), 481–494 (1966).
- <sup>46</sup>C. Norberg, "Flow around rectangular cylinders: Pressure forces and wake frequencies," *J. Wind Eng. Ind. Aerodyn.* **49**(1–3), 187–196 (1993).
- <sup>47</sup>F. Farassat, "Derivation of formulations 1 and 1A of Farassat," NASA TM-2007-214853, 2007.
- <sup>48</sup>Y. He, "Aerodynamic noise simulation of high-speed train bogie," Ph.D. thesis, University of Southampton, 2023.
- <sup>49</sup>S. C. Morris, "Shear-layer instabilities: Particle image velocimetry measurements and implications for acoustics," *Annu. Rev. Fluid Mech.* **43**, 529–550 (2011).
- <sup>50</sup>N. Curle, "The influence of solid boundaries upon aerodynamic sound," *Proc. R. Soc. London* **231**(1187), 505–514 (1955).